



ECAMP: Entity-centered Context-aware Medical Vision Language Pre-training

Rongsheng Wang^{a,b,f,1}, Qingsong Yao^{c,1}, Zihang Jiang^{a,b,*}, Haoran Lai^{a,b,f}, Zhiyang He^f, Xiaodong Tao^f, S. Kevin Zhou^{a,b,d,e,*}

^aSchool of Biomedical Engineering, Division of Life Sciences and Medicine, University of Science and Technology of China (USTC), Hefei Anhui, 230026, China

^bCenter for Medical Imaging, Robotics, Analytic Computing & Learning (MIRACLE), Suzhou Institute for Advance Research, USTC, Suzhou Jiangsu, 215123, China

^cStanford University, Palo Alto, California, 94025, United States

^dKey Laboratory of Intelligent Information Processing of Chinese Academy of Sciences (CAS), Institute of Computing Technology, CAS

^eKey Laboratory of Precision and Intelligent Chemistry, USTC, Hefei Anhui, 230026, China

^fAnhui IFLYTEK CO., Ltd.

ARTICLE INFO

Article history:

Keywords: Medical Vision-language Pre-training, Masked Modeling, cross-modality Learning

ABSTRACT

Despite significant advancements in medical vision-language pre-training, existing methods have largely overlooked the inherent linguistic complexity and imbalanced issue within medical reports, as well as the complex cross-modality contextual relationships between texts and images. To close this gap, we propose a novel Entity-centered Context-aware Medical Vision-language Pre-training (ECAMP) framework, which establishes a more entity-centered, context-sensitive, and balanced understanding of medical reports to effectively pre-train the vision encoder. We first distill entity-centered context from medical reports utilizing large language models, enabling ECAMP to draw more precise supervision from the text modality. By further incorporating entity-aware re-balanced factor and descriptor masking strategies into masked language modeling, ECAMP significantly enhances the knowledge of entities within the reports. A context-guided super-resolution task is proposed alongside a multi-scale context fusion design to improve the semantic integration of both coarse and fine-level image representations, which prompts better performance for multi-scale downstream applications. ECAMP integrates these innovations together, leading to significant performance leaps over current state-of-the-art methods and establish a new standard for cross-modality pre-training in medical imaging. The effectiveness of ECAMP is demonstrated by extensive experiments on various domains and organs, which achieves cutting-edge results on multiple tasks including classification, segmentation, and detection across 5 public chest X-ray and 4 funduscopy datasets respectively.

© 2025 Elsevier B. V. All rights reserved.

1. Introduction

By virtue of its exceptional accuracy and efficiency, deep learning (DL) is increasingly pivotal in medical image analysis Zhou et al. (2021); Pathak et al. (2022); Esteva et al. (2017); Erickson et al. (2017); Titano et al. (2018). However, precision is

contingent upon large-scale and high-quality annotations, which require an extensive number of experienced medical professionals, rendering it a costly endeavor. Fortunately, the diagnosis and experiential knowledge Pellegrini et al. (2023) of doctors are preserved in the form of paired reports and images, which provide valuable semantic context for training DL-based models. More notably, these supervised signals are relatively accessible at little to no additional costs.

Cutting-edge algorithms Bannur et al. (2023); Ye et al. (2024) in medical vision-language pre-training (Med-VLP) primarily

*Corresponding authors: skevinzhou@ustc.edu.cn (S Kevin Zhou) and jzh0103@ustc.edu.cn (Z Jiang).

¹Equal contribution.

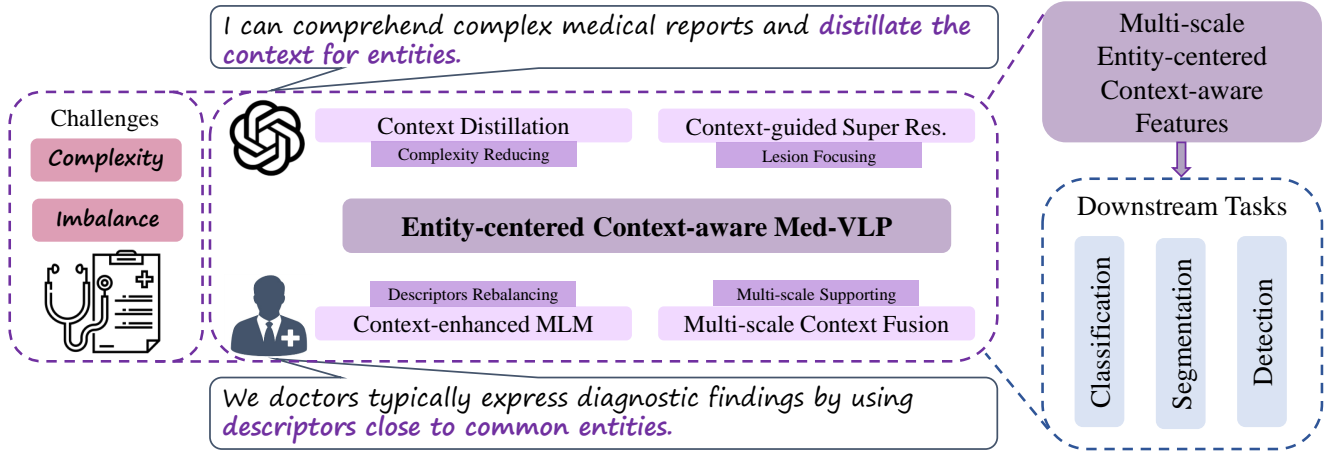


Fig. 1: Our ECAMP is designed to learn representative and multi-scale features from complex and imbalanced medical reports, extracting medical knowledge from both ChatGPT and experts, with a particular focus on entities such as diseases, symptoms, and others. *Context distillation* prompts ChatGPT to distillate precise content for entities, thereby reducing the complexity of reports, while *Context-enhanced MLM* predicts the masked descriptors close to entities and addresses the imbalance difficulty caused by doctors' habits. *Context-guided Super Resolution* focuses the model on anatomy area, concentrating the target pathology textures and locations. Further, ECAMP develops *Multi-scale Context Fusion* to learn global and local projections simultaneously to support multi-granularity downstream tasks.

leverage the information-rich medical report-image pairs to learn generic representations from two aspects: *contrastive-based* methods align the text and image features at both global Zhang et al. (2020) and local Huang et al. (2021); Wang et al. (2022); Li et al. (2024) levels; while *reconstruction-based* methods generate the masked words Devlin et al. (2018) and image patches He et al. (2021) using cross-modality information Zhou et al. (2023a).

Nevertheless, these methods still exhibit limitations in harnessing the potential of supervision in the context of the report. First, the linguistic challenge Li et al. (2019) posed by complex biomedical context Li et al. (2018) impedes the effectiveness of pre-training Boecking et al. (2022). Second, doctors often include diagnoses for common diseases (e.g., pneumothorax) in their reports, even when these diseases are negative Dai et al. (2021). This practice leads to a significant context imbalance issue Boecking et al. (2022): the majority of disease diagnoses are negative. We extract and count the two adjective words before disease entities (defined as “descriptors”) and plot the statistics of these descriptors in Fig. 2 (b), which clearly indicate an imbalance: the ‘is no’ descriptor is dominant and the imbalance ratio between negative (e.g., “is no”) and positive (e.g., “there is”) descriptors reaches 20:1. This imbalance injects an adverse bias into the optimization of masked language modeling (MLM) Devlin et al. (2018) and complicates the model’s ability to accurately learn the semantics of the positive diseases.

In this paper, we introduce **Entity-Centered Context-Aware Medical vision-language Pre-training (ECAMP)**, a robust pre-training framework for 2D medical images. As shown in Fig. 1, the main contribution of ECAMP is pre-training representative and multi-scale features from complex and imbalanced medical reports through a cohesive integration of four synergistic modules. ECAMP consists of four simple-yet-effective components: 1) *entity-aware context distillation*, 2) *entity-centered context-enhanced MLM*, 3) *context-guided super-resolution*, and 4) *multi-scale context fusion*. We propose a cohesive integration

of four modules, which contribute from different perspectives with close collaboration, emphasizing an entity-centered and context-aware design.

Unlike PRIOR Cheng et al. (2023) that substitutes complex biomedical sentences with prototypes, we propose *entity-aware context distillation* to distill semantic context using Large Language Model, leveraging its strong power in linguistic comprehensive and summarization OpenAI (2023). Based on our consultations with medical professionals Dai et al. (2021), doctors typically express diagnostic findings by using descriptors close to Medical Subject Headings (MeSH) Lipscomb (2000) entities (e.g., pneumonia). Our key observations related to medical reports motivate the need for better distilling the semantic contexts related to clinically-relevant entities from reports. Specifically, we use ChatGPT Brown et al. (2020) to summarize the complex reports into succinct expressions with entity diagnosis (like “There may be pneumonia.”). We construct an entity list, including diseases and symptoms, and further generate more precise and simplified descriptions of disease existence and severity, which facilitate more effective supervision of the complex reports in pre-training. To the best of our knowledge, we are the first to leverage the power of large language models for medical vision-language pre-training, which attempts to explicitly address the challenge of information overload in clinically dense reports. The distilled context is not just a simplified report; it contains more precise descriptions of the existence and severity of diseases, enabling our model to learn more precise anatomical locations and disease-related features from the complex reports.

Despite that multi-modal MLM has been investigate in recent Med-VLP methods such as M3AE Chen et al. (2022) and MRM Zhou et al. (2023a), they randomly mask portions of the report for construction, which overlook the importance and imbalance of the descriptive words beyond the entity. Accordingly, we propose *entity-centered context-enhanced MLM* strategy. The *descriptor masking* employs a fixed masking strategy to optimize the pre-trained model to predict these key descriptors for

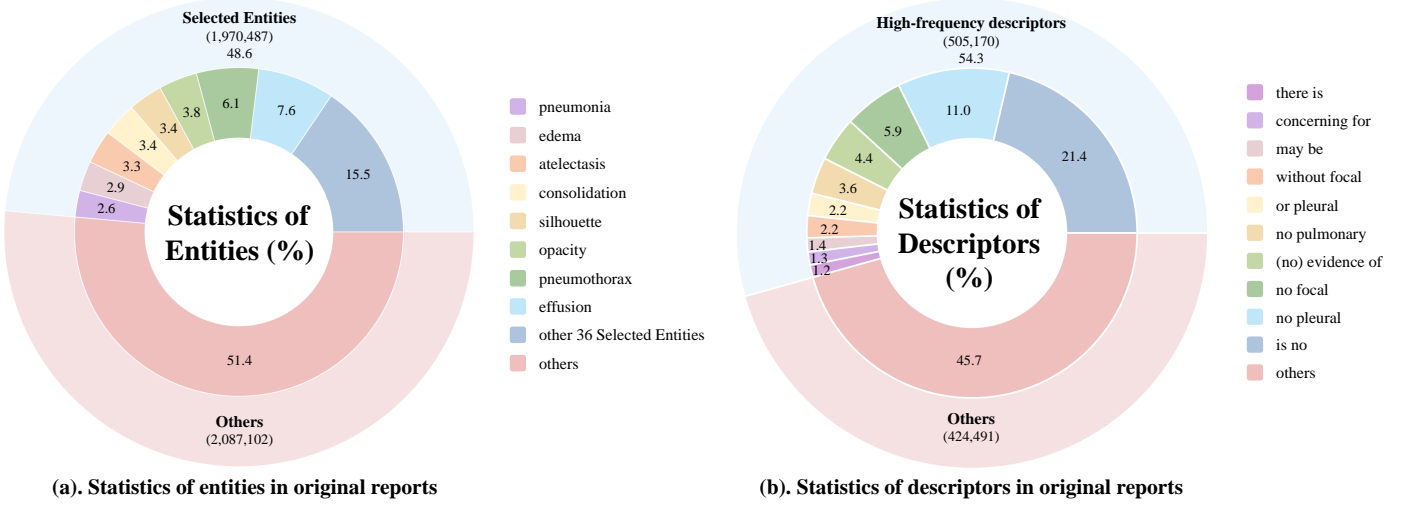


Fig. 2: The statistics of high-frequency entities and descriptors in the original reports of MIMIC-CXR Johnson et al. (2019a). We merge other low-frequent words as “others”. Our selected entities account for approximately 48.6% of the overall occurrences. The imbalance ratio between negative (e.g., “is no”) and positive (e.g., “there is”) descriptors reaches to 20:1.

better modeling the semantics of entities and context. To tackle the imbalance problem (as shown in Fig 2 (b).), we further add an effective *re-balancing factor* for less-appearing positive descriptors, which prevents the model from ignoring the critical positive diagnoses in reports.

Moreover, traditional MIM methods, such as MAE He et al. (2021), treat each patch of the image equally during loss computation. However, lesions usually locate at small area of imaging. Super-resolution exhibits promise as a lesion focus and reinforcement of masked image modeling in self-supervised proxy task Zhou et al. (2023a). Given that critical pathology usually occupies small patches, we hypothesize that learning to reconstruct these subtle cues help to better understand pathology and hence lead to better performance. Fortunately, leveraging the concise distilled reports, we can retrain patch-level contrastive-based methods Huang et al. (2021) to procure precise entity-specific attention maps. These maps facilitate our proposed *context-guided super-resolution* to learn the high-resolution characteristics of the target pathology with broader contextual information, thereby enabling a more holistic and accurate interpretation of medical images based on the entities and context.

In addition, we find current cross-modal reconstruction-based methods typically employ either global average pooling (GAP) Zhou et al. (2023a) or cross-attention Chen et al. (2022) to integrate global and local vision representations to assist MLM. In contrast, we introduce *multi-scale context fusion* to aggregate global and local projection of pre-trained vision encoder simultaneously. Multi-scale feature aggregation is definitely a trend for Med-VLP, but different methods has special designs which fit their frameworks. GLORIA Huang et al. (2021), which uses contrastive learning to aggregate and align multi-scale features in two different branch. Instead, the only supervision which contains diagnosis information in our framework comes from masked report reconstruction, the gradient is propagated to local and global features via addition and duplication simultaneously, and train the multi-scale features. Our motivation is to learn both global and local informative representations, which can be

generalized to a wide range of multi-scale downstream tasks, including classification, segmentation, and detection.

To comprehensively and thoroughly validate the effectiveness, We pre-train our medical pre-training method ECAMP on MIMIC-CXR Johnson et al. (2019a) and FFA-IR Li et al. (2021b) dataset consisting of image-report pairs for both Chest X-rays and fundoscopies. Extensive experiments are conducted on multi-scale downstream tasks (including classification, segmentation, and detection) across multiple public datasets. The experimental results across various domains and organs demonstrate the superiority and generalization of ECAMP to outperform a plethora of competitive state-of-the-art (SOTA) Med-VLP methods with significant performance gaps. In sum, ECAMP with its readily accessible components prove valuable in fortifying the establishment of pre-training framework for medical foundation model. Codes and models are available at <https://github.com/ToniChopp/ECAMP>.

2. Related Work

2.1. General Vision Language Pre-training

Vision-language pre-training (VLP) aims to improve the performance of multi-granularity downstream vision and language tasks by pre-training the model on large-scale image-text pairs. Tremendous success has been achieved in recent literature, which can be summarized into two groups: encoder-based Li et al. (2021a, 2020a), or encoder-decoder based Cho et al. (2021); Wang et al. models. One of the most representative encoder-based methods is CLIP Radford et al. (2021), which shows a great potential for learning mutual information between visual and linguistic data. Recently, more works (e.g. GLIP Li et al. (2022b), SLIP Mu et al. (2022), FLIP Li et al. (2022c), OSCAR Li et al. (2020b), and VinVL Zhang et al. (2021)) indicate that fine-grained context alignment facilitates the model to learn more representative representations. For the encoder-decoder methods, BLIP Li et al. (2022a) leverages a decoder to reconstruct text by leveraging vision semantic context. In this paper,

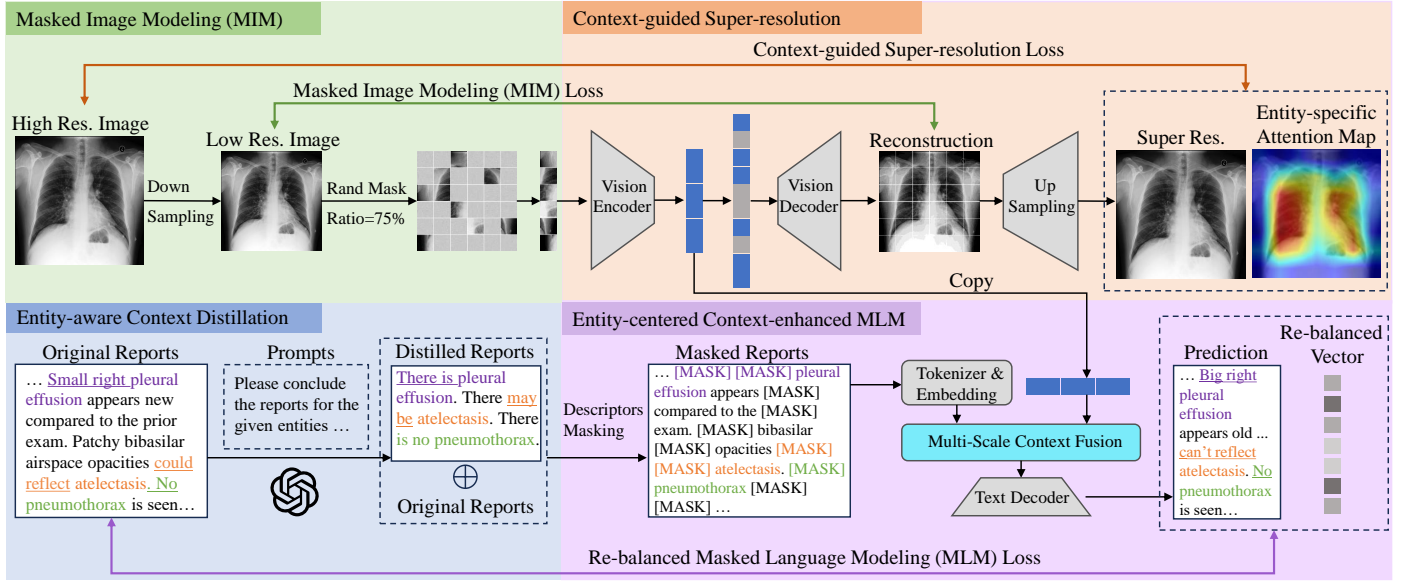


Fig. 3: The overall framework of our ECAMP. Initially, *entity-aware context distillation* succinctly encapsulates precise diagnosis for each entity. Then *entity-centered context-enhanced MLM* masks the two descriptive words (underlined) preceding the entities, employing a re-balancing vector to direct the model’s attention towards critical minority-positive expressions. To further enhance the learning of pathology vision contexts, *context-guided super-resolution* utilizes an entity-specific attention map. Finally, we introduce a novel *multi-scale context fusion* block (highlighted in cyan) to concurrently capture representative global and local features.

we focus on the challenging medical domain, where medical report is harder to comprehend and accuracy is more of paramount importance.

2.2. Medical Vision Language Pre-training

Recent Med-VLP methods can be categorized into two distinct types: report-supervised cross-modal alignment pre-training and reconstruction-based self-supervised pre-training. The groundbreaking works of the former type such as ConVIRT Zhang et al. (2020), REFERS Zhou et al. (2022), and CheXZero Tiu et al. (2022) pre-train the model by directly maximizing mutual information between the global representations. GLORIA Huang et al. (2021), SAT Liu et al. (2023a), and MGCA Wang et al. (2022) propose to align fine-grained features of paired image patches and words. PRIOR Cheng et al. (2023) and BioVIL Boecking et al. (2022) attempt to comprehend intricate medical reports. MedKLIP Wu et al. (2023) and KAD Zhang et al. (2023c) extract the medical-related information using a triplet extraction module as additional supervised signals. FLAIR Silva-Rodriguez et al. (2023) integrates the expert’s domain knowledge in the form of descriptive textual prompts. RETFound Zhou et al. (2023b) provides a basis for better label-efficient model adaptation. Inspired by BERT Devlin et al. (2018) and MAE He et al. (2021), the latter type learns representation by cross-modal context reconstruction task. M3AE Chen et al. (2022) utilizes cross-attention for integrating multi-modal information to reconstruct masked tokens. While MRM Zhou et al. (2023a) directly applies global average pooling for fusing visual features for masked text modeling. Further, MPMA Zhang et al. (2023a) introduces a memory-augmented cross-modal fusion module to fully integrate visual information to assist report reconstruction.

Advanced efforts try to combine contrastive-based and reconstruction-based pre-training. CMITM Chen et al. (2023) contrastively aligns global report and image representations after pre-training with MRM Zhou et al. (2023a), while MedIM Xie et al. (2023) boosts MGCA Wang et al. (2022) with attention

guided masked image modeling. Med-Unic Wan et al. (2023) and Med-MLLM Liu et al. (2023b) further improve the performance by leveraging more pre-training datasets. Pair-Aug Xie et al. (2024a) proposes pairwise augmentation to improve performance without introducing extra datasets. Notwithstanding the enhancements, the aforementioned approaches are constrained by the intricacies of comprehending biomedical reports and the imbalance in diagnoses, which has spurred our pursuit of developing ECAMP.

2.3. Large Language Models (LLMs)

Compared to BERT Devlin et al. (2018), recent LLMs such as GPT-3 Brown et al. (2020) have a much larger scale in terms of training data and model parameters. This scale affords them robust zero-shot generalization capabilities to comprehend previously unseen contexts. Further, instruction-tuning Ouyang et al. (2022); Sanh et al. (2022) is proposed to effectively improve the performance of LLM in novel application scenarios, including news summarization Zhang et al. (2023b) and code summarization Su and Mcmillan (2023). Luckily, advanced LLMs such as ChatGPT Brown et al. (2020) also exhibit robust capabilities in complex biomedical contexts. To the best of our knowledge, we are among the first few works to distill medical knowledge from medical reports using LLMs.

3. Method

In this section, we take CXRs and corresponding reports as an example to illustrate our proposed method. We first introduce how ECAMP leverages *context distillation* to distill distinct context from LLM in section 3.1. Then, we illustrate the basic masked image modeling (MIM) He et al. (2021) and the proposed *entity-centered context-enhanced MLM* in section 3.2. Next, section 3.3 shows the process of *context-guided super-resolution*. Finally, we clarify the detailed approaches of *multi-*

Table 1: Our selected entities. We select 44 entities based on their importance and frequency of appearance in radiology reports as comprehensively as possible.

Entities			
abnormality	abscess	aerate	aorta
atelectasis	bronchiectasis	calcification	cardiomediastinal
cardiomegaly	catheter	chf	collapse
congestion	consolidation	contour	COPD
deformity	dilation	distention	edema
effusion	embolism	emphysema	engorgement
fibrosis	fracture	granuloma	hernia
hilar	hyperinflated	hemidiaphragm	infiltrate
mass	nodule	obscure	opacity
perihilar	pneumonia	pneumothorax	sarcoidosis
silhouette	thickening	tuberculosis	vasculature

scale context fusion in section 3.4 to integrate both global and local vision features for MLM.

3.1. Context Distillation

Given an image $I^o \in \mathbb{R}^{H^o \times W^o}$ and its original paired report T_o , our target is to extract concise diagnosis for diseases from T_o . Accordingly, we select the set of entities $R = \{r^1, r^2, \dots, r^k\}$ from MeSH Lipscomb (2000), representing the diseases of interest in chest radiography. For each original report T_o , we identify entities \mathbf{r}_o mentioned in the report through string matching. We manually curate a list of 44 entities, as shown in Table 1, including diseases, symptoms and anatomical locations. These entities are sourced from MeSH Lipscomb (2000) and selected based on their importance and the frequency of appearance in radiology reports. As illustrated in Fig. 2 (a), the 44 entities selected for this study account for approximately 48.6% of the overall occurrences. Next, prompt p is designed to require LLM to comprehend the complex biomedical context and summarize the diagnosis for disease entities \mathbf{r}_o . Furthermore, to make the summarization of LLM stable, we leverage in-context learning Min et al. (2022) to construct an one-shot Wei et al. (2021) sample p' in the final prompt $p = P(T_o, \mathbf{r}_o, p')$. Table 2 displays the prompt utilized for report distillation. By inputting the radiology report as the content to ChatGPT OpenAI (2023) with this specific prompt, we obtain a distilled report that includes more detailed semantics regarding the existence and severity of entities. Specifically, by using GPT3.5-turbo API OpenAI (2023) and setting temperature with 0 to generate 10,000 distilled reports, to save API call, we train a Vicuna7B Chiang et al. (2023) to further distill all the reports. Examples of these distilled reports are presented in Table 3. ² The distilled report T_d is finally computed as follows:

$$T_d = \text{LLM}(P(T_o, \mathbf{r}_o, p')). \quad (1)$$

3.2. Masked Image and Language Modeling

Masked image modeling We first decompose the original image I^o into high-resolution $I^h \in \mathbb{R}^{H^h \times W^h}$ and low-resolution $I^l \in \mathbb{R}^{H^l \times W^l}$ input. The low-resolution image I^l is split into N_p^l patches with size $P \times P$. Following MAE He et al. (2021), we

mask a large ratio (75%) of the N_p^l low-resolution patches, resulting in the unmasked patches $I_u = \{I_u^1, I_u^2, \dots, I_u^{N_u^l}\}$ and masked patches $I_m = \{I_m^1, I_m^2, \dots, I_m^{N_m^l}\}$. Then the patch embedding E_p is obtained by linearly projecting the flattened unmasked patches I_u . Vision transformer Dosovitskiy et al. (2020) (ViT) is chosen as the vision encoder E_l , which projects the patch embedding E_p along with its positional embedding E_{pos} as the vision feature $f_v = E_l(I_u, E_{pos})$. In the image decoding procedure, f_v is fed into an image decoder D_l after recovering to the original N_p size, resulting in reconstructed image $\hat{I}^l = D_l(E_l(I_u))$. We choose mean square error (MSE) loss to optimize the reconstructed image:

$$\mathcal{L}_{\text{MIM}}(\hat{I}^l, I_m) = \text{MSE}(D_l(E_l(I_u)), I_m). \quad (2)$$

Table 2: Our prompt used for report distillation is designed to include both an indication and an example. Providing ChatGPT OpenAI (2023) with an example of the task helps enhance its performance in generating distilled reports.

```

Messages = [
  { "role": "system", "content": f""
    You are a knowledgeable and veteran doctor.
    "" },
  { "role": "user", "content": f""
    Please help me analysis the medical reports and conclude them briefly. Now, I
    will give you a medical report, as well as the mentioned entities. Please write
    brief and clear conclusions according to the reports as the following format:
    'There is [a] [b].': when you are sure whether the entity exists in the report, or
    'There may [a] [b].': when you are not sure whether the entity exists in the report.
    [a] represents adjective words describing the severeness or existence of the entity
    [b]. Please generate conclusions for the entities mentioned above one by one,
    according to the format and do not generate other words. Please keep only one
    entity in a sentence, there is no need of using 'and' or 'or' to connect two or more
    words.
    "" },
  { "role": "user", "content": f""
    —Example—
    Report: As compared to ~, the lung volumes have slightly decreased. Signs
    of mild over inflation and moderate pleural effusion persist. Elongation of the
    descending aorta.
    Entities: aorta, inflation, effusion
    Conclusion:
    There is moderate pleural effusion.
    There is mild over inflation.
    There is descending aorta.
    —Example END—
    Given the report: {report}
    Entities: {entity}.
    Conclusion:
    "" },]

```

Entity-centered context-enhanced MLM For the paired report T_o , we concatenate the distilled report T_d as the text input $T = [T_o, T_d]$. As shown in Fig. 2 (b), we mark the first β words preceding the entity R as “descriptive words” $T_a = \{t_a^1, t_a^2, \dots, t_a^{N_a^T}\}$. Based on practical experience, the majority of descriptive words used by doctors are located within the first two words preceding the entity words, e.g., “There is mild pneumonia.”, we set β to 2. Instead of using random masking Zhou et al. (2023a); Chen et al. (2022); Devlin et al. (2018), ECAMP introduces a naive-yet-effective “descriptors masking” to mask the tokens of descriptive words, compelling the network to predict the diagnosis of the doctors for each entity. The remaining words are randomly masked with a ratio of 75% to get masked words $T_m = \{t_m^1, t_m^2, \dots, t_m^{N_m^T}\}$ and unmasked words T_u , and the masked words are replaced with [MASK] for training. WordPiece Wu et al. (2016) is chosen as tokenizer to convert T into text tokens. Text embeddings E_t are further computed

²A medical student is tasked with evaluating the accuracy of the context distillation. The average distillation accuracy for ChatGPT 3.5 turbo is 93.6%, while the accuracy for our Vicuna 7B is 93.2%.

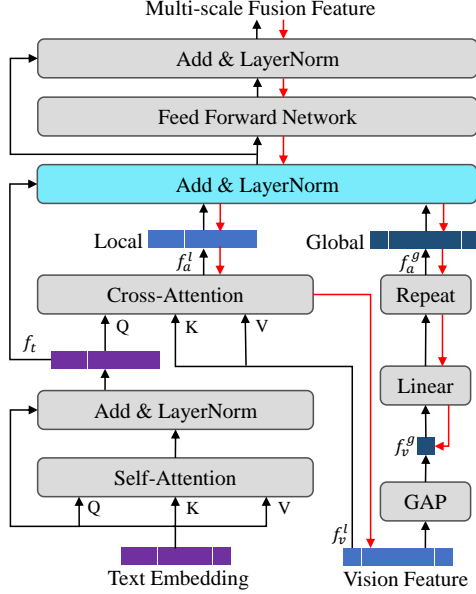


Fig. 4: The framework of *multi-scale context fusion*. The addition operation (highlighted in cyan) concurrently fuses the text feature, local aggregated vision feature, and global vision feature. The red arrows indicate the propagation of gradients, which simultaneously flow toward both global and local vision features.

by projecting the text tokens and adding the encoded position information.

A high text masking ratio challenges the model to reconstruct the reports by encoding the vision context thoroughly and accurately. Accordingly, a novel *multi-scale context fusion* module (MSCF, see section 3.4) is proposed to integrate the vision feature and text embedding $f_f = \text{MSCF}(f_v, E_t)$. The reconstructed text \hat{T} is generated by decoding the fused feature f_f using a BERT-based Devlin et al. (2018) text decoder $\hat{T} = D_t(f_f)$. The MLM loss for each masked word $t \in [T_m, T_a]$ is defined as $\mathcal{L}_{\text{MLM}}^t(\hat{t}, t) = -\log(P(\hat{t} = t))$.

Moreover, we simply categorize T_a into two groups: negative descriptions T_{neg} and others T_{oth} , with N_{neg}^T and N_{oth}^T words, respectively. Please note that since the expressions of positive descriptors are diverse, we divide them into others T_{oth} . To better facilitate the pre-training model to learn precise disease semantics, we focus on modeling the minority-positive disease descriptions instead of majority-negative words, technically, we multiply the loss of T_{neg} by a small number λ_{neg} , and the loss of N_{oth}^T by λ_{oth} , where

$$\lambda_{\text{neg}} * N_{\text{neg}}^T + \lambda_{\text{oth}} * N_{\text{oth}}^T = N_a^T. \quad (3)$$

According to the statistical results in Fig. 2 (b), the most negative descriptor “there is no” occurs approximately 20× more often than the most positive descriptor “there may be.”, so we set $\lambda_{\text{neg}} = 0.05$. Please note that λ_{oth} is important to make sure that the model pays an enough attention to accurately reconstruct the critical “descriptive words” T_a . The final loss of entity-centered

context-aware MLM is defined:

$$\begin{aligned} \mathcal{L}_{\text{MLM}} = & \sum_j^{N_m^T} \mathcal{L}_{\text{MLM}}^t(\hat{t}_m^j, t_m^j) + \sum_j^{N_{\text{neg}}^T} \lambda_{\text{neg}} \mathcal{L}_{\text{MLM}}^t(\hat{t}_{\text{neg}}^j, t_{\text{neg}}^j) \\ & + \sum_j^{N_{\text{oth}}^T} \lambda_{\text{oth}} \mathcal{L}_{\text{MLM}}^t(\hat{t}_{\text{oth}}^j, t_{\text{oth}}^j). \end{aligned} \quad (4)$$

3.3. Context-guided Super-resolution

Using the entity-centered distilled report T_d , we re-train the SOTA fine-grained representation contrastive learning method GloRIA Huang et al. (2021) to generate entity-specific attention map A for image I^h . Then, an up-sampling module D_{SR} up-scales the reconstructed image \hat{I}^l to the high-resolution results \hat{I}^h , which consists of a bi-linear interpolation and two convolution layers with a residual connection. As the model should focus on generating disease-relevant visual textures, we use the attention map as the guidance for super-resolution (SR). The SR loss function is as follows:

$$\mathcal{L}_{\text{SR}}(\hat{I}^h, I^h) = \text{MSE}(D_{\text{SR}}(D_I(E_I(I_u))), I^h|A), \quad (5)$$

The overall loss function of ECAMP is:

$$\mathcal{L} = \mathcal{L}_{\text{MIM}} + \mathcal{L}_{\text{MLM}} + \mathcal{L}_{\text{SR}}. \quad (6)$$

3.4. Multi-scale Context Fusion

Different from MRM Zhou et al. (2023a) which directly adds the vision feature f_v to the text embedding E_t , we first apply a self-attention (SA) for an initial comprehension of text embedding $f_t = \text{SA}(E_t)$. In order to simultaneously attain representative global and local features for multi-scale downstream tasks, we leverage patch-wise vision features f_v as local vision features f_v^l and use global average pooling (GAP) to compute global vision feature $f_v^g = \text{GAP}(f_v^l)$. Next, we aggregate local vision context f_v^l with text feature f_t by cross-attention (CA) to generate local aggregated feature $f_a^l = \text{CA}(f_v^l, f_t)$, and project the f_v^g by a linear projector to obtain global feature f_a^g . Finally, we integrate text feature f_t , local aggregated feature f_a^l , and duplicate global feature f_a^g by addition. During the pre-training stage, the only supervision which contains diagnosis information in our framework comes from MLM loss (Eq. 4). So, as shown in Fig. 4, the gradient is propagated to local vision feature f_v^l and global vision feature f_v^g via addition and duplication simultaneously, and train the multi-scale features.

Fine-tuning stage: ECAMP takes the full images as input without masking in this stage. Our multi-scale context fusion design enables the model to learn compact global representation as well as informative fine-level local representation. For the high-level downstream task like classification, we fine-tune the global vision feature f_v^g . For the low-level vision tasks including segmentation and detection, we fine-tune the local vision features f_v^l . Thanks to the expressive representation, we are able to achieve impressive performance across different level vision tasks.

Table 3: Examples of report distillation are presented. For each report, we showcase how the semantics of our selected entities are distilled by ChatGPT and our Vicuna-7B. The entities are highlighted in multiple colors for clarity. The distilled reports provide more specificity regarding the existence of entities.

Original	There is mild left base atelectasis seen on the frontal view without clear correlation on the lateral view. No definite focal consolidation is seen. There is no pleural effusion or pneumothorax . The aorta is slightly tortuous. The cardiac silhouette is not enlarged. There is no overt pulmonary edema , mild left base atelectasis . otherwise, no acute cardio pulmonary process.
ChatGPT	There is mild left base atelectasis . There is a slightly tortuous aorta . There is no pleural effusion . There is no pneumothorax . There is no overt pulmonary edema . There is no acute cardio pulmonary process.
Vicuna-7B	There is mild left base atelectasis . There is no pleural effusion . There is no pneumothorax . There is no definite focal consolidation . There is no enlarged cardiac silhouette . There is no overt pulmonary edema .
Original	In comparison with the study of __, the increased opacification at the right base has essentially cleared with better inspiration. Cardiac silhouette remains at the upper limits of normal in size and there is again tortuosity of the aorta without vascular congestion or pleural effusion . Bi-apical changes especially on the right are stable.
ChatGPT	There is tortuosity of the aorta . There is no pleural effusion . There is no vascular congestion . There is no change in the bi-apical changes. There is stable increased opacification at the right base. The cardiac silhouette is at the upper limits of normal in size.
Vicuna-7B	There is tortuosity of the aorta . There is no pleural effusion . There is no vascular congestion .
Original	Pa and lateral chest radiographs again demonstrate severe hyperinflation and diffuse bronchiectasis . There is no focal consolidation , pleural effusion or pneumothorax . The cardiomeastinal silhouette is stable. No acute cardio pulmonary process. Findings were relayed to Dr __.
ChatGPT	There is severe hyperinflation . There is diffuse bronchiectasis . There is no focal consolidation . There is no pleural effusion . There is no pneumothorax . The cardiomeastinal silhouette is stable. There is no acute cardio pulmonary process.
Vicuna-7B	There is severe hyperinflation . There is diffuse bronchiectasis . There is no focal consolidation . There is no pleural effusion . There is no pneumothorax .
Original	The lung volumes are normal. Mild cardiomegaly which is stable. Normal hilar and mediastinal structures. No pneumonia . No pulmonary edema . No pleural effusion . Status post cabg with aligned median sternotomy wires and normal location of surgical clips. Status post right lung surgery with surgical material seen. Mild cardiomegaly . No evidence of pneumonia .
ChatGPT	There is normal hilar . There is mild cardiomegaly . There is no pneumonia . There is no pulmonary edema . There is no pleural effusion . There is status post CABG with aligned median sternotomy wires. There is status post right lung surgery with surgical material. The lung volumes are normal.
Vicuna-7B	There is normal hilar . There is mild cardiomegaly . There is no pneumonia . There is no pulmonary edema . There is no pleural effusion .
Original	3 radiographs are provided. On the film, 3 the tip of the dobbhoff catheter projects over the proximal parts of the stomach. The course of the device is unremarkable. No complications. Unchanged appearance of the lung parenchyma the pleural and the heart.
ChatGPT	There is no complication with the Dobbhoff catheter . There is unchanged appearance of the lung parenchyma. There is no pleural abnormality. There is no heart abnormality. There is no disease.
Vicuna-7B	There is no disease.

4. Experiment

4.1. Pre-training Dataset

MIMIC-CXR 2.0.0³ Johnson et al. (2019a,b) contains 377,110 chest radiographs and 227,835 corresponding reports. Each report may be associated with one or more images captured from frontal, back, and lateral views. We extract detailed descriptions of medical diseases by focusing on the impression and finding sections in the free-text reports.

FFA-IR⁴ Li et al. (2021b) includes 10,790 reports along with 1,048,584 Fundus Fluorescein Angiography (FFA) images from clinical practice. It comprises explainable annotations, based

on a schema of 46 categories of lesions; and it is bilingual, providing both English and Chinese reports for each case. We select English reports and paired FFA images as pre-training data. This setup is used to evaluate the performance of pre-training frameworks on funduscopy images.

4.2. Downstream Tasks Datasets

ChestX-ray14⁵ Wang et al. (2017) comprises 112,120 frontal-view chest radiographs, and introduces a multi-label classification task involving *14 common chest pathologies*. The dataset is officially split into training, validation, and testing subsets with a ratio of 70%/10%/20%.

³<https://physionet.org/content/mimic-cxr/2.0.0/>

⁴<https://physionet.org/content/ffa-ir-medical-report/1.0.0/>

⁵<https://nihcc.app.box.com/v/ChestXray-NIHCC>

Table 4: Evaluating our method against other SOTA Med-VLP approaches on the fine-tuning classification task. † denotes we reproduce results using their officially released models. Methods with # leverage disease-level annotations. The best and second-best results are **bolded** and underlined.

Method	ChestX-ray14 (AUC)			CheXpert (AUC)			RSNA (AUC)			COVIDx (ACC)		
	1%	10%	100%	1%	10%	100%	1%	10%	100%	1%	10%	100%
Random init	60.0	65.2	72.8	70.4	81.1	85.8	71.9	82.2	88.5	64.2	75.4	87.7
ImageNet init	69.8	74.4	80.0	80.1	84.8	87.6	83.1	87.3	90.8	72.0	84.4	90.3
<i>CNN-based</i>												
GLoRIA Huang et al. (2021)	70.7	78.6	84.1	86.6	87.8	88.1	86.1	88.0	88.6	73.3	86.8	90.5
†SAT Liu et al. (2023a)	67.4	79.3	83.7	86.3	88.0	88.2	86.7	87.5	89.0	75.0	88.5	94.3
PRIOR Cheng et al. (2023)	75.7	79.4	84.3	86.2	88.3	88.6	85.7	87.1	89.2	<u>79.5</u>	89.8	94.8
MedKLIP# Wu et al. (2023)	77.2	78.9	83.2	87.1	88.4	88.6	87.3	88.0	89.3	78.3	88.8	95.3
KAD Zhang et al. (2023c)	78.7	80.7	82.5	87.2	88.2	88.5	89.8	91.8	92.5	78.5	90.5	<u>95.8</u>
<i>ViT-based</i>												
MAE He et al. (2021)	74.7	81.3	85.1	80.7	86.0	86.7	84.2	89.6	91.3	69.8	82.3	90.8
GLoRIA Huang et al. (2021)	77.7	82.8	85.0	86.5	87.5	87.8	89.7	91.2	92.1	76.8	<u>91.8</u>	94.8
REFERS Zhou et al. (2022)	76.7	80.9	84.7	87.2	88.1	88.2	89.4	91.6	92.7	76.5	<u>90.8</u>	94.5
MGCA# Wang et al. (2022)	78.2	82.7	85.0	87.0	88.4	88.5	90.7	92.6	<u>93.4</u>	75.2	91.5	94.3
MRM Zhou et al. (2023a)	79.4	<u>84.0</u>	<u>85.9</u>	<u>88.5</u>	<u>88.5</u>	<u>88.7</u>	91.3	<u>92.7</u>	<u>93.3</u>	78.0	90.3	92.5
ECAMP (Ours)	81.9	85.1	86.7	88.8	89.5	89.7	91.5	93.2	94.2	83.0	95.5	97.5

Table 5: Comparison with other state-of-the-art methods on the linear probe classification task. † means performances in ChestX-ray14 Wang et al. (2017) and methods like MRM Zhou et al. (2023a) are fine-tuned using their official released models. Methods with # leverage disease-level annotations, while Med-UniC Wan et al. (2023) uses external additional pre-training data. The best and second-best results are **bolded** and underlined.

Method	†ChestX-ray14 (AUC)			CheXpert (AUC)			RSNA (AUC)			COVIDx (ACC)		
	1%	10%	100%	1%	10%	100%	1%	10%	100%	1%	10%	100%
Random init	52.1	54.6	55.3	56.1	62.6	65.7	58.9	69.4	74.1	50.5	60.3	70.0
ImageNet init	67.0	67.5	71.6	74.4	79.7	81.4	74.9	74.5	76.3	64.8	78.8	86.3
<i>CNN-based</i>												
SAT Liu et al. (2023a)	74.4	79.2	81.8	86.9	88.3	88.6	87.4	89.2	90.2	74.5	84.8	89.3
†PRIOR Cheng et al. (2023)	74.9	79.5	82.1	86.3	86.7	87.3	88.2	90.4	90.7	74.8	85.0	89.8
MedKLIP# Wu et al. (2023)	78.5	80.9	83.2	86.2	86.5	87.7	88.1	90.8	92.0	74.5	85.3	90.3
†KAD Zhang et al. (2023c)	78.1	79.8	81.6	86.4	86.9	87.8	87.9	90.0	91.3	75.0	84.3	90.5
Med-UniC Wan et al. (2023)	-	-	-	88.2	89.2	89.5	89.1	90.4	90.8	76.5	89.0	92.8
<i>ViT-based</i>												
MAE He et al. (2021)	75.1	79.7	82.9	82.4	84.6	85.2	86.5	89.7	90.2	79.0	88.5	92.5
GLoRIA Huang et al. (2021)	77.0	81.9	83.8	84.6	85.8	86.2	87.2	88.1	88.9	73.3	87.7	92.1
MGCA# Wang et al. (2022)	78.7	82.7	84.1	88.8	89.1	<u>89.7</u>	89.1	89.9	90.8	74.8	84.8	92.3
†MRM Zhou et al. (2023a)	<u>78.8</u>	<u>82.7</u>	<u>84.6</u>	88.1	88.1	88.3	<u>90.9</u>	<u>92.5</u>	<u>92.5</u>	<u>79.8</u>	89.0	92.8
MedIM-C Xie et al. (2023)	-	-	-	88.9	89.3	<u>89.7</u>	-	-	-	<u>77.2</u>	<u>90.3</u>	<u>93.6</u>
MLIP# Li et al. (2024)	-	-	-	89.0	89.4	90.0	89.3	90.0	90.8	75.3	86.3	92.5
ECAMP (Ours)	81.0	83.8	85.1	89.3	89.5	<u>89.7</u>	91.4	92.9	93.5	86.3	95.0	96.0

CheXpert⁶ Irvin et al. (2019) includes 223,648 chest radiographs from a frontal or lateral view, which categorizes each image into 5 diseases: atelectasis, cardiomegaly, consolidation, edema, and pleural effusion. Aligned with Zhang et al. (2020); Huang et al. (2021), we designate the expert-labeled official validation set as the test data. We randomly choose 5,000 radiographs from the training data as the validation set. The split for training/validation/testing comprises 218,414/5,000/234 images.

RSNA Pneumonia (RSNA)⁷ Shih et al. (2019) is composed of 29,700 frontal-view chest radiographs, each accompanied by pneumonia opacity bounding boxes if pneumonia is present in the image. Four tasks are conducted on this dataset: fine-tune classification, linear classification, semantic segmentation, and object detection. For fine-tune and linear classification tasks,

we adhere to the official data partitioning, allocating 25,184, 1,500, and 3,000 images for the training, validation, and test sets, respectively. In the context of semantic segmentation and object detection, our approach aligns with the methodology proposed in Wang et al. (2022), wherein the original training set is randomly divided into subsets of 16,010/5,337/5,337 samples for training/validation/testing purposes, respectively.

COVIDx CXR-3 (COVIDx)⁸ Wang et al. (2020) comprises 29,986 chest radiographs. This dataset presents a multi-class classification task, categorizing each image into *COVID-19*, *non-COVID pneumonia*, or *normal*. In line with Wang et al. (2022); Wan et al. (2023); Chen et al. (2023), version 6 of this dataset is used. The official validation set is considered as our test data, and simultaneously, 10% of the original training set is randomly selected as validation data.

⁶<https://stanfordmlgroup.github.io/competitions/chexpert/>

⁷<https://www.rsna.org/rsnai/ai-image-challenge/rsna-pneumonia-detection-challenge-2018>

⁸<https://www.kaggle.com/datasets/andyczhao/covidx-cxr2/versions/7>

Table 6: Comparison with other state-of-the-art methods fine-tuned on semantic segmentation and object detection task. † denotes performances reproduced using their officially released models. Methods with # leverage disease-level annotations, while Med-UniC Wan et al. (2023) uses additional pre-training data. The best and second-best results are **bolded** and underlined.

Method	SIIM (Dice)			RSNA (Dice)			RSNA (mAP)		
	1%	10%	100%	1%	10%	100%	1%	10%	100%
Random init	9.0	28.6	54.3	6.9	10.6	18.5	1.0	4.0	8.9
ImageNet init	10.2	35.5	63.5	34.8	39.9	64.0	3.6	8.0	15.7
<i>CNN-based</i>									
MedKLIP# Wu et al. (2023)	50.2	60.8	63.9	66.2	69.4	71.9	8.9	16.3	24.5
KAD Zhang et al. (2023c)	35.8	46.9	63.4	59.3	67.5	67.8	9.8	14.8	18.8
SAT Liu et al. (2023a)	59.2	68.2	74.7	67.8	74.8	75.3	10.6	19.1	22.0
PRIOR Cheng et al. (2023)	54.6	63.7	76.8	68.7	71.9	74.4	13.8	20.5	25.6
MGCA# Wang et al. (2022)	49.7	59.3	64.2	63.0	68.3	69.8	12.9	16.8	24.9
Med-Unic Wan et al. (2023)	56.7	62.2	64.4	72.6	74.4	76.7	16.6	<u>22.3</u>	<u>31.1</u>
MLIP# Li et al. (2024)	51.6	60.8	68.1	67.7	68.8	73.5	<u>17.2</u>	19.1	25.8
<i>ViT-based</i>									
†MGCA# Wang et al. (2022)	62.7	65.2	71.4	75.2	<u>77.8</u>	<u>78.3</u>	8.9	19.2	26.3
†MRM Zhou et al. (2023a)	<u>63.1</u>	<u>68.3</u>	78.4	74.2	<u>77.6</u>	<u>78.2</u>	11.5	20.3	27.1
Med-Unic Wan et al. (2023)	62.1	67.3	71.5	<u>75.6</u>	76.6	77.9	-	-	-
MedIM-C Xie et al. (2023)	-	63.5	81.3	-	-	-	-	-	-
MedIM Xie et al. (2024b)	-	64.2	82.0	-	-	-	-	-	-
ECAMP (Ours)	67.3	70.8	84.5	77.1	78.6	79.5	19.8	28.0	31.6

SIIM-ACR Pneumothorax (SIIM)⁹ Steven G. Langer and George Shih (2019) introduces the task of pneumothorax segmentation for evaluating the performance of segmentation models. This dataset includes 12,047 frontal-view chest radiographs with meticulously manually labeled pneumothorax masks. In accordance with Huang et al. (2021), we partition the dataset into training/validation/test sets with a ratio of 70%/15%/15%.

ODIR-5K¹⁰ consists of 5,000 patient records, each containing color fundus photographs of both the left and right eyes, along with corresponding diagnostic keywords provided by clinicians. These keywords are categorized into eight distinct classes. We utilize the official test set as the test data. Additionally, 639 images are randomly selected as validation data, resulting in a data split of 70% for training, 10% for validation, and 20% for testing.

APTOS-2019¹¹ Karthik (2019) presents a multi-class classification task for determining the severity level of diabetic retinopathy (DR) in fundus images. The dataset comprises 3,662 labeled images, with DR severity levels ranging from 0 to 4. The dataset is randomly partitioned into training, validation, and test sets with a split ratio of 70%/10%/20%, respectively.

MuReD¹² Rodríguez et al. (2022) consists of 2,451 multi-label retinal fundus images covering 20 categories. We randomly select 222 images from the official training set to serve as our validation data. The official test set is used for testing data. The data is split into 70% for training, 10% for validation, and 20% for testing.

RIGA¹³ Ji et al. (2021) introduces the task of retinal cup and disc segmentation, containing a total of 750 color fundus images from three sources. We adopt the official test set, with the dataset

split into 590 images for training, 95 for validation, and 95 for testing.

4.3. Metrics

AUC and ACC are used for multi-label and multi-class classification, respectively. Specifically, we calculate the average AUC for each class. **Dice** is commonly measured for segmentation tasks, we set the threshold to 0.5 as default for all experiments. **mAP** is adopted for object detection. Following Wang et al. (2022), we set the IOU thresholds to 0.4, 0.45, 0.5, 0.55, 0.6, 0.65, 0.7, 0.75, and report the average precision.

4.4. Implementation Details

We utilize an 8-layer ViT-B/16 Dosovitskiy et al. (2020) as the backbone for the image encoder and a 4-layer ViT-B/16 for the image decoder. Additionally, we employ BERT Devlin et al. (2018) as the text encoder. If not otherwise stated, we resize images to 224×224 as input, except for super-resolution supervision we retain the 448×448 resolution images. Texts are padded or truncated to a fixed length of 256 tokens. The latent dimension, denoted as D, is set to 768. The implementation is based on PyTorch Paszke et al. (2019). For pre-training on MIMIC-CXR Johnson et al. (2019a,b), our framework runs for 120 epochs on 4 A100 GPUs, taking approximately 20 hours. The training batch size is set to 256 for each GPU, and we utilize a gradient accumulation step of 8. Consequently, the effective batch size reaches 8,192. For pre-training on FFA-IR Li et al. (2021b), our framework runs for 60 epochs on 4 A100 GPUs, taking approximately 15 hours. Other settings are the same with the pre-training stage on CXRs. We opt for AdamW Loshchilov and Hutter (2017) as our default optimizer, with a learning rate of 1.5e-4 and weight decay of 0.05. The values for β_1 and β_2 are set to 0.9 and 0.95. The mean squared error (MSE) loss is employed for masked image modeling and super-resolution, while cross-entropy loss is used for masked language modeling.

⁹<https://www.kaggle.com/c/siim-acr-pneumothorax-segmentation>

¹⁰<https://odir2019.grandchallenge.org/>

¹¹<https://www.kaggle.com/datasets/mariaherrero/apotos2019>

¹²<https://data.mendeley.com/datasets/pc4mb3h8hz/1>

¹³https://deepblue.lib.umich.edu/data/concern/data_sets/3b591905z

For the LLM in Eq. 1, we use GPT-3.5-turbo API OpenAI (2023) with temperature setting to 0 to distill 10,000 reports and fine-tune a Vicuna model Chiang *et al.* (2023) to distill the rest of the reports.

4.5. Baselines

We conduct a comprehensive comparative analysis of ECAMP with numerous SOTA Med-VLP approaches *pre-trained solely on MIMIC-CXR* using ResNet-50 He *et al.* (2016) (‘CNN-Based’) or ViT-B/16 Dosovitskiy *et al.* (2020) (‘ViT-Based’) as backbone, including MAE He *et al.* (2021) trained on ImageNet Krizhevsky *et al.* (2017) (denoted as ‘ImageNet init’), GLORIA Huang *et al.* (2021), REFERS Zhou *et al.* (2022), SAT Liu *et al.* (2023a), PRIOR Cheng *et al.* (2023), MedKLIP Wu *et al.* (2023), MGCA Wang *et al.* (2022), KAD Zhang *et al.* (2023c), MedIM-C Xie *et al.* (2023), MRM Zhou *et al.* (2023a), MedIM Xie *et al.* (2024b) and MLIP Li *et al.* (2024). Notably, Med-UniC Wan *et al.* (2023) uses external multilingual datasets. In addition, for fair comparison, we pre-train MAE He *et al.* (2021) (denoted as ‘MAE’) and GLORIA Huang *et al.* (2021) with ViT-B/16 on MIMIC-CXR Johnson *et al.* (2019a) using official source code. For MGCA, MRM, SAT, PRIOR, KAD, and MedKLIP whose official model are released, we fine-tune their models on the public downstream datasets in case there is no corresponding performance metrics in referenced papers. For MedIM-C, Med-UniC, MedIM and MLIP, whose official models are absent, we directly copy the performances from their papers for comparison. For extensive experiments on FFA images, we reproduce MAE He *et al.* (2021), GLORIA Huang *et al.* (2021) and MRM Zhou *et al.* (2023a) using their official code pre-trained on FFA-IR Li *et al.* (2021b) dataset, which is under the same settings as our ECAMP.

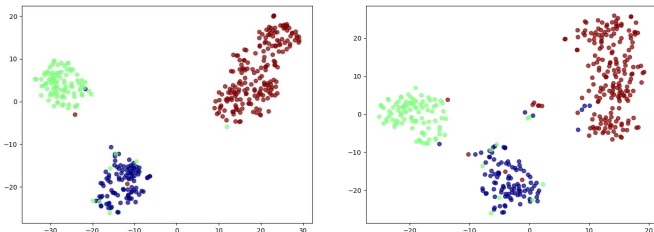


Fig. 5: T-SNE visualizations of ECAMP and MRM Zhou *et al.* (2023a) in the fine-tuning classification task on COVIDx Wang *et al.* (2020) dataset. The left panel represents ECAMP, while the right panel shows MRM. The blue points correspond to images labeled as “no pneumonia”, the green points represent image features related to “pneumonia”, and the red points indicate “COVID-19” features.

5. Results

5.1. Results on Classification

We conduct both fine-tune and linear-probe with our ECAMP on four datasets, using 1%, 10%, and 100% of the training data, respectively. As in Table 4, our ECAMP significantly outperforms *all* CNN and ViT-based competitive Med-VLP models across different ratios of training data on the four datasets.

It is worth noting that, on the ChestX-ray14 Wang *et al.* (2017), *which encompasses the most of testing data and disease labels,*

ECAMP surpasses the strongest counterpart by 2.5% using only 1% labeled data. Surprisingly, on the COVIDx with a novel disease “COVID-19”, which is not present in MIMIC-CXR Johnson *et al.* (2019a), a great performance gap can be found in Table 4 between ECAMP and SOTA methods. COVIDx dataset includes the RSNA pneumonia dataset as well as a collection of chest X-rays featuring COVID-19 cases, which is similar to pneumonia. So, the pre-trained method has to learn different textures of pneumonia to further classify the COVID-19 of normal pneumonia. As shown in Fig. 5, we use t-SNE to visualize the features of our ECAMP and MRM. It is evident that our model demonstrates a better separation of features across “no pneumonia”; “pneumonia”, and “COVID-19”, which supports the superiority of pre-trained features of our ECAMP method and possibly enables better generalizability to novel class. This validates the superiority of the representation learned by our ECAMP. Interestingly, we find the cross-modality reconstruction-based methods MRM Zhou *et al.* (2023a) and our ECAMP outperform the contrastive-based methods like MGCA Wang *et al.* (2022) and GLORIA Huang *et al.* (2021). Moreover, Table 5 presents the results of linear-probe classification. ECAMP exhibits consistently improved performance compared with SOTA methods on ChestX-ray14, RSNA and COVIDx datasets. To evaluate the generalizability and adaptability of ECAMP, we extend the pre-training framework to Fundus Fluorescein Angiography (FFA) images and corresponding textual reports. Comprehensive experiments on fine-tuning classification is presented in Table 10. We perform fine-tuning for both multi-label and multi-class classification. As the table shows, our proposed ECAMP method substantially outperforms all state-of-the-art ViT-based medical vision-language pre-training approaches, even when applied beyond the CXR image domain. Notably, on the ODIR-5K dataset, which includes labels representing a broad spectrum of fundus diseases, ECAMP achieves a 5% improvement over the strongest competing method, despite utilizing only 1% of the labeled data.

5.2. Results on Segmentation and Detection

To assess the effectiveness of local representations learned by ECAMP, extensive experiments on fine-grained downstream tasks including segmentation and detection are conducted in Table 6. Compared to strong SOTA approaches and boosted by MSCF, ECAMP makes remarkable improvements on all three datasets and ratios. Even in scenarios where MGCA Wang *et al.* (2022) and MedKLIP Wu *et al.* (2023) leverage disease-level labels, and Med-UniC Wan *et al.* (2023) incorporates additional large-scale training data like PadChest Bustos *et al.* (2020), our ECAMP consistently outperforms all aforementioned methods. Distinguished Dice score leaps of 4.2% and 1.5% against SOTA methods are achieved on two segmentation datasets SIIM Steven G. Langer and George Shih (2019) and RSNA Shih *et al.* (2019) using 1% training data, respectively. Notably, ECAMP reaches a Dice score of 67.3%, which outperforms CNN-based methods fine-tuned using all training data on SIIM Steven G. Langer and George Shih (2019). Similarly, our method attains the best mAP using limited data on the object detection task. Remarkably, our method exhibits a significant lead of 8.3% compared to other SOTA open-source methods based on ViT. These achievements

Table 7: Ablation study of five simple-yet-effective components (*context distillation (CD)*, *descriptors masking (DM)*, *re-balancing factor (RF)*, *context-guided super-resolution (SR)*, and *MSCF*) proposed in ECAMP on multi-scale downstream tasks including fine-tune classification (ChestX-ray14 Wang et al. (2017)), linear classification (COVIDx Wang et al. (2020)), semantic segmentation (SIIM Steven G. Langer and George Shih (2019)), and object detection (RSNA Shih et al. (2019)). All of the downstream tasks are trained with **1%**, **10%** and **100%** of training data.

CD	DM	RF	SR	MSCF		ChestX-ray14 (AUC)			COVIDx (ACC)			SIIM (Dice)			RSNA (mAP)		
				Global	Local	1%	10%	100%	1%	10%	100%	1%	10%	100%	1%	10%	100%
×	×	×	×	✓	✓	79.5	83.9	86.0	78.0	87.3	92.3	65.4	68.6	80.7	4.1	20.6	26.0
✓	×	×	×	✓	✓	80.2	84.2	86.1	81.5	89.0	89.5	65.9	69.2	81.2	12.2	22.4	26.6
✓	✓	×	×	✓	✓	80.8	84.4	86.2	82.1	90.3	92.8	66.0	69.4	82.4	13.9	23.3	27.3
✓	✓	✓	×	✓	✓	81.5	84.7	86.5	83.0	92.3	95.0	66.6	69.9	83.6	16.1	24.5	29.1
×	✓	✓	✓	✓	✓	81.3	84.6	86.3	82.5	92.5	95.0	66.9	69.9	84.1	15.6	25.2	29.7
✓	×	✓	✓	✓	✓	81.4	84.5	86.2	83.0	94.0	95.3	66.4	70.0	83.4	16.8	25.7	30.5
✓	✓	×	✓	✓	✓	80.8	84.1	86.2	82.8	91.8	92.5	66.6	69.8	84.0	16.9	26.5	30.3
✓	✓	✓	✓	✓	×	81.8	85.0	86.4	85.0	92.5	94.5	65.7	69.5	83.6	12.6	21.7	28.6
✓	✓	✓	✓	×	✓	81.4	84.7	86.1	83.3	88.0	90.8	67.5	70.7	84.3	20.4	28.2	31.7
✓	✓	✓	✓	✓	✓	81.9	85.1	86.7	86.3	95.0	96.0	67.3	70.8	84.5	19.8	28.0	31.6

Table 8: Ablation study on the impact of two critical components: *Entity Selection Strategy* and *Text Input Composition*. We compare three entity selection strategies: (1) **Top-20** highest-frequency clinical entities, (2) **Top-10%** frequency-percentile cutoff, and (3) our proposed method leveraging the **Top-44** most frequent entities. For text input composition, we assess four paradigms: (1) original radiology reports alone (**Origin-alone**), (2) ChatGPT-distilled reports alone (**Dis-alone**), (3) hybrid inputs combining original reports with named entity recognition (NER)-based distilled reports (**Hybrid-NER**), and (4) hybrid inputs combining original reports with ChatGPT-distilled reports (**Hybrid-GPT**). These configurations are evaluated on multi-scale downstream tasks including fine-tune classification (ChestX-ray14 Wang et al. (2017)), linear classification (COVIDx Wang et al. (2020)), semantic segmentation (SIIM Steven G. Langer and George Shih (2019)), and object detection (RSNA Shih et al. (2019)). All of the downstream tasks are trained with **1%**, **10%** and **100%** of training data.

Entity Selection	Text Input Composition	ChestX-ray14 (AUC)			COVIDx (ACC)			SIIM (Dice)			RSNA (mAP)		
		1%	10%	100%	1%	10%	100%	1%	10%	100%	1%	10%	100%
Top-20	Hybrid-GPT	81.2	84.7	86.4	84.8	92.8	94.5	66.7	70.6	82.5	13.3	25.3	26.9
Top-10%	Hybrid-GPT	80.5	84.0	86.3	83.5	90.5	93.3	66.6	70.6	83.1	17.1	25.6	28.0
Top-44	Origin-alone	81.3	84.6	86.3	82.5	92.5	95.0	66.9	69.9	84.1	15.6	25.2	29.7
Top-44	Dis-alone	80.8	84.2	86.2	82.0	91.0	94.5	67.1	69.6	84.3	15.3	25.4	29.4
Top-44	Hybrid-NER	81.7	84.9	86.6	84.0	93.8	95.3	66.9	70.1	84.2	16.2	25.9	30.4
Top-44	Hybrid-GPT	81.9	85.1	86.7	86.3	95.0	96.0	67.3	70.8	84.5	19.8	28.0	31.6

Table 9: Ablation study on parameter λ_{neg} proposed in Eq. 3 on fine-tuning (ChestX-ray14 Wang et al. (2017)) and linear (COVIDx Wang et al. (2020)) classification with different ratios of training data (1%, 10%, and 100%).

λ_{neg}	ChestX-ray14 (AUC)			COVIDx (ACC)		
	1%	10%	100%	1%	10%	100%
0.025	81.7	84.5	86.5	85.0	93.3	94.8
0.05	81.9	85.1	86.7	86.3	95.0	96.0
0.1	81.8	84.6	86.4	80.5	94.8	95.3
0.25	81.5	84.2	86.2	79.5	94.0	94.5
0.5	81.4	84.2	86.2	82.5	91.5	91.8

substantiate the effectiveness of ECAMP to optimize informative local features for fine-grained downstream tasks. Table 11 presents the results of our fine-grained downstream task for retinal cup and disc segmentation on RIGA Ji et al. (2021) dataset when pre-trained on FFA images and paired reports. Here, the average Dice coefficient is recorded as the primary metric. Our proposed method, ECAMP, consistently outperforms all previously mentioned approaches on this task, demonstrating its superior performance. Through extensive experiments conducted on FFA images, we have validated that ECAMP effectively leverages its strong capability to utilize contextual information and capture multi-granularity cross-modality relationships between text and images. This enables ECAMP to generalize well across different medical vision tasks, making it a robust and highly effective medical vision-language pre-training method.

5.3. Ablation Study and Analysis

Advantages of context distillation The first row in Table 7 is trained by basic MIM and MLM. When we use the distilled easy-comprehensible report, we observe a performance improvement of 3.5% on COVIDx Wang et al. (2020) and 0.7% on ChestX-ray14 Wang et al. (2017) while using 1% training data. Moreover, when we train ECAMP without the distilled report, notable performance degradation is observed, particularly on COVIDx and RSNA Shih et al. (2019), validating the significant role of *entity-aware context distillation*.

Effectiveness of descriptors masking After constantly masking the critical descriptive words (as shown in Fig. 3) preceding the entities, substantial performance enhancements are observed across both coarse-grained and fine-grained tasks, exceeding our initial expectations (as shown in Table 7). Accordingly, it is confirmed that *descriptors masking* can better leverage the supervised signals in medical reports.

Sensitive analysis of the re-balancing factor In the performance increment between the 3rd and the 4th rows as well as the 7th row and the last row of Table 7, we highlight the effectiveness of our proposed *re-balancing factor*. The AUC score increases by 1.1% and 1.0% respectively on ChestX-ray14 Wang et al. (2017), and the ACC shows sequential improvements of 3.5% and 3.2% when utilizing 1% and 10% of training data. It is evident that the *re-balancing factor* primarily contributes to the performance of classification tasks, and is also effective on fine-grained tasks. We further provide hyper-parameter analy-

Table 10: Comparison with other state-of-the-art medical vision language pre-training methods typically designed for CXRs pre-trained on FFA images and fine-tuned on disease classification tasks. † denotes performances reproduced using their officially released codes pre-trained on FFA-IR Li et al. (2021b) dataset. The best and second-best results are **bolded** and underlined.

Method	ODIR-5K (AUC)			APTOS (ACC)			MuRed (AUC)	
	1%	10%	100%	1%	10%	100%	10%	100%
Random init	54.1	57.5	65.7	59.7	63.4	68.5	51.1	66.5
ImageNet init	62.6	64.0	77.4	68.3	71.7	75.0	52.9	70.7
<i>ViT-based</i>								
†MAEHe et al. (2021)	63.8	72.9	82.4	71.8	<u>75.0</u>	79.9	68.8	82.9
†GLoRIAHuang et al. (2021)	<u>67.4</u>	74.1	87.2	72.3	<u>74.9</u>	<u>81.0</u>	81.0	<u>93.5</u>
†MRMZhou et al. (2023a)	66.8	<u>78.3</u>	<u>88.1</u>	<u>73.9</u>	74.3	<u>80.9</u>	<u>82.1</u>	93.0
ECAMP (Ours)	71.8	81.2	90.0	75.9	76.9	83.2	85.6	94.5

Table 11: Comparison with other SOTA medical vision language pre-training methods pre-trained on FFA images and fine-tuned for retinal cup and disc segmentation task. The average Dice of retinal cup and disc is shown. † denotes performances reproduced using their officially released codes pre-trained on FFA-IR Li et al. (2021b) dataset. The best and second-best results are **bolded** and underlined.

Method	RIGA (Dice)		
	1%	10%	100%
Random init	50.9	65.0	78.3
ImageNet init	63.3	73.8	82.5
<i>ViT-based</i>			
†MAE He et al. (2021)	67.0	78.1	86.4
†GLoRIA Huang et al. (2021)	78.1	82.3	<u>92.4</u>
†MRM Zhou et al. (2023a)	<u>83.6</u>	<u>88.3</u>	92.1
ECAMP (Ours)	84.6	88.7	92.6

sis of λ_{neg} corresponding to different imbalance ratios between positive and negative expressions. As shown in Table 9, setting λ_{neg} to 0.05 according to the imbalance ratio (20:1) leads to the best performance. These results strongly demonstrate the effectiveness of re-balanced factor and its capability of encouraging pre-training model to learn precise disease semantics.

Performance of context-guided SR As listed in the 4th row and the last row of Table 7, employing *context-guided SR* provides performance gains from 83.0% to 86.3% and 92.3% to 95.0% on COVIDx. Notably, on SIIM, the Dice score improves by 0.7% and 0.9%, mAP sees a notable increase of 3.7% and 3.5% on RSNA while using 1% and 10% ratio, which validates its effectiveness in learning informative features by generating detailed pathology vision context. This underscores the efficacy of *context-guided super resolution* in aiding pre-trained models to capture prior knowledge of visual texture structure, particularly enhancing performance in fine-grained visual downstream tasks.

Contributions of MSCF We exclusively integrate the global vision feature f_v^g and local aggregated feature f_a^l to predict the masked words respectively. The results in Table 7 validate that, only fusing f_v^g decreases the performances on low-level downstream tasks (segmentation and detection), while the classification performance relies on well-trained f_a^l . It is confirmed that *MSCF* successfully contributes to learning local and global representations and concurrently achieving SOTA performance on multi-scale downstream tasks.

Entity selection strategies We conduct systematic ablation studies to evaluate the impact of *entity selection strategies*. As illustrated in Table 8, we compare three entity selection strategies: (1) Top-20 highest-frequency entities, (2) Top-10% frequency-

percentile cutoff, and (3) our proposed method leveraging the Top-44 most frequent entities (as shown in Table 1). Compared to our method using 44 selected entities, strategies relying on the Top-20 entities or Top-10% frequency thresholds exhibit diminished performance in modeling disease-related features, particularly under low-data fine-tuning scenarios.

Text input composition As our approach pre-trains vision encoder through the supervision of masked language modeling, text input composition may determine the performance of pre-trained models. For text input composition, we assess four paradigms: (1) original radiology reports alone, (2) ChatGPT-distilled reports alone, (3) hybrid inputs combining original reports with named entity recognition (NER) Jain et al. (2021) -based distilled reports, and (4) hybrid inputs combining original reports with ChatGPT-distilled reports. As shown in the last four rows of 8, using ChatGPT-distilled reports alone as input leads to significant performance degradation. While distilled reports capture disease existence and severity, they omit critical visual symptom descriptors, potentially impairing the model’s ability to localize fine-grained anatomical features. Hybrid inputs combining original and distilled reports yield more robust performance, as they balance structured context with raw textual detail.

We conduct further ablation study on context distillation method using the structured template “[entity_1] has [entity_2]” with Radgraph-based NER annotations Jain et al. (2021). Comparing the last two rows of Table 8, NER-based distillation method, though effective for entity presence/absence labeling, is less adept at capturing nuanced clinical relationships in complex reports. This limitation is evidenced by the limited improvement in multi-scale context-aware tasks, especially in fine-grained anatomical location-related tasks (e.g., segmentation and detection). In contrast, ChatGPT-based distillation method preserves nuanced clinical descriptors such as disease severity, anatomical location, and temporal progression (Table 3). Quantitative results demonstrate that our approach more effectively models disease severity and anatomical interactions, strongly supporting our hypothesis that ChatGPT-driven context distillation better preserves implicit clinical knowledge.

5.4. Representation analysis

As the attention map of the local vision feature and the corresponding distilled reports visualized in Fig. 6, the text modality of ECAMP captures the correct pathological regions of lung collapse (marked by red boxes) through cross-modal attention

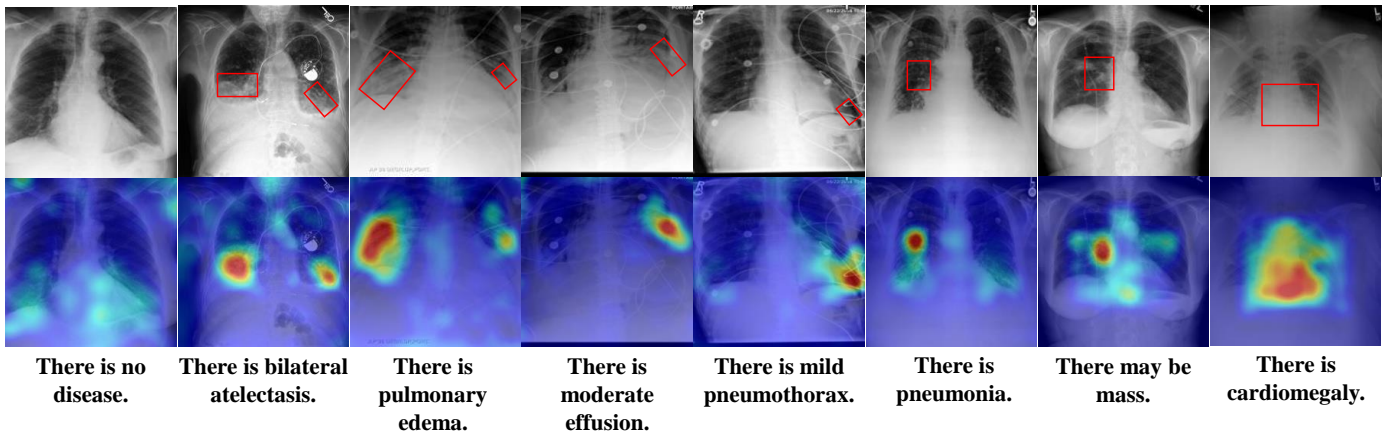


Fig. 6: Cross-attention maps between diagnosis and vision patterns learned by local aggregated features in MSCF, which successfully localizes the pathology region of various diseases.

with the visual modality. Furthermore, there is no particularly disease-sensitive cross-attention for healthy images. These results support the ability of the *MSCF* to learn accurate and discriminative fine-grained representations, which is crucial for improving the performance of local downstream tasks.

6. Impact, Limitation, and Conclusion

In this paper, we propose a novel pre-training method which extracts representative and multi-scale features from complex and imbalanced medical reports. Our method is a cohesive integration of four modules, which contribute from different perspectives with close collaboration, emphasizing an entity-centered and context-aware design. We confront the linguistic challenge of complex medical reports by distilling precise entity-centered knowledge using a large language model. Subsequently, the catastrophic context-imbalanced issue is addressed by proposing a novel re-balancing factor, then entity-centered descriptors masking is proposed to strengthen the entity-centered context for masked language modeling. Furthermore, a context-guided super-resolution learns to capture the critical pathology vision features with entity-awareness. In addition, multi-scale context fusion helps to optimize informative global and local representations simultaneously. These four readily accessible modules form the core of our simple-yet-effective general Med-VLP framework, referred to as ECAMP, whose significant superior performance is validated on various public datasets across CXRs and fundoscopies on downstream tasks, including classification, segmentation, and detection. ECAMP facilitates the development of a robust medical foundation model, ultimately alleviating the workload of experts. However, the absence of explicit alignment between text and vision modalities hinders the application in zero-shot setting. In the future, we plan to incorporate contrastive learning to further empower ECAMP to function as an expert doctor without any manual annotation.

7. Acknowledgments

This work was supported by National Natural Science Foundation of China under Grant 62271465, Suzhou Basic Research Program under Grant SYG202338, and Open Fund Project of

Guangdong Academy of Medical Sciences, China (No. YKY-KF202206).

References

- Bannur, S., Hyland, S., Liu, Q., Perez-Garcia, F., Ilse, M., Castro, D.C., Boecking, B., Sharma, H., Bouzid, K., Thieme, A., et al., 2023. Learning to exploit temporal structure for biomedical vision-language processing, in: CVPR, pp. 15016–15027.
- Boecking, B., Usuyama, N., Bannur, S., de Castro, D.C., Schwaighofer, A., Hyland, S.L., Wetscherek, M.T.A., Naumann, T., Nori, A., Alvarez-Valle, J., Poon, H., Oktay, O., 2022. Making the most of text semantics to improve biomedical vision-language processing, in: ECCV.
- Brown, T., Mann, B., Ryder, N., Subbiah, M., Kaplan, J.D., Dhariwal, P., Neelakantan, A., Shyam, P., Sastry, G., Askell, A., et al., 2020. Language models are few-shot learners, pp. 1877–1901.
- Bustos, A., Pertusa, A., Salinas, J.M., de la Iglesia-Vayá, M., 2020. Padchest: A large chest x-ray image dataset with multi-label annotated reports. *Medical image analysis* 66, 101797.
- Chen, C., Zhong, A., Wu, D., Luo, J., Li, Q., 2023. Contrastive masked image-text modeling for medical visual representation learning, Springer. pp. 493–503.
- Chen, Z., Du, Y., Hu, J., Liu, Y., Li, G., Wan, X., Chang, T.H., 2022. Multi-modal masked autoencoders for medical vision-and-language pre-training, Springer. pp. 679–689.
- Cheng, P., Lin, L., Lyu, J., Huang, Y., Luo, W., Tang, X., 2023. Prior: Prototype representation joint learning from medical images and reports, in: ICCV, pp. 21361–21371.
- Chiang, W.L., Li, Z., Lin, Z., Sheng, Y., Wu, Z., Zhang, H., Zheng, L., Zhuang, S., Zhuang, Y., Gonzalez, J.E., Stoica, I., Xing, E.P., 2023. Vicuna: An open-source chatbot impressing gpt-4 with 90%* chatgpt quality. URL: <https://lmsys.org/blog/2023-03-30-vicuna/>.
- Cho, J., Lei, J., Tan, H., Bansal, M., 2021. Unifying vision-and-language tasks via text generation, in: International Conference on Machine Learning, PMLR. pp. 1931–1942.
- Dai, S., Wang, Q., Lyu, Y., Zhu, Y., 2021. Bdkg at medqa 2021: System report for the radiology report summarization task, in: Proceedings of the 20th Workshop on Biomedical Language Processing, pp. 103–111.
- Devlin, J., Chang, M.W., Lee, K., Toutanova, K., 2018. Bert: Pre-training of deep bidirectional transformers for language understanding.
- Dosovitskiy, A., Beyer, L., Kolesnikov, A., Weissenborn, D., Zhai, X., Unterthiner, T., Dehghani, M., Minderer, M., Heigold, G., Gelly, S., et al., 2020. An image is worth 16x16 words: Transformers for image recognition at scale, in: ICLR.
- Erickson, B.J., Korfiatis, P., Akkus, Z., Kline, T.L., 2017. Machine learning for medical imaging. *Radiographics* 37, 505–515.
- Esteva, A., Kuprel, B., Novoa, R.A., Ko, J., Swetter, S.M., Blau, H.M., Thrun, S., 2017. Dermatologist-level classification of skin cancer with deep neural networks. *nature* 542, 115–118.
- He, K., Chen, X., Xie, S., Li, Y., Doll'ar, P., Girshick, R.B., 2021. Masked autoencoders are scalable vision learners, in: CVPR, pp. 15979–15988.

- He, K., Zhang, X., Ren, S., Sun, J., 2016. Deep residual learning for image recognition, in: Proceedings of the IEEE conference on computer vision and pattern recognition, pp. 770–778.
- Huang, S.C., Shen, L., Lungren, M.P., Yeung, S., 2021. Gloria: A multimodal global-local representation learning framework for label-efficient medical image recognition, in: ICCV, pp. 3942–3951.
- Irvine, J., Rajpurkar, P., Ko, M., Yu, Y., Ciurea-Ilcus, S., Chute, C., Marklund, H., Haghighi, B., Ball, R., Shpanskaya, K., et al., 2019. Chexpert: A large chest radiograph dataset with uncertainty labels and expert comparison, in: Proceedings of the AAAI conference on artificial intelligence, pp. 590–597.
- Jain, S., Agrawal, A., Saporta, A., Truong, S., Duong, D.N.D., Bui, T., Chambon, P., Zhang, Y., Lungren, M., Ng, A., Langlotz, C., Rajpurkar, P., Rajpurkar, P., 2021. Radgraph: Extracting clinical entities and relations from radiology reports, in: Vanschoren, J., Yeung, S. (Eds.), Proceedings of the Neural Information Processing Systems Track on Datasets and Benchmarks, Curran. URL: https://datasets-benchmarks-proceedings.neurips.cc/paper_files/paper/2021/file/c8ffe9a587b126f152ed3d89a146b445-Paper-round1.pdf.
- Ji, W., Yu, S., Wu, J., Ma, K., Bian, C., Bi, Q., Li, J., Liu, H., Cheng, L., Zheng, Y., 2021. Learning calibrated medical image segmentation via multi-rater agreement modeling, in: Proceedings of the IEEE/CVF Conference on Computer Vision and Pattern Recognition (CVPR), pp. 12341–12351.
- Johnson, A.E., Pollard, T.J., Berkowitz, S.J., Greenbaum, N.R., Lungren, M.P., Deng, C.Y., Mark, R.G., Horng, S., 2019a. Mimic-cxr, a de-identified publicly available database of chest radiographs with free-text reports. Scientific data 6, 1–8.
- Johnson, A.E., Pollard, T.J., Greenbaum, N.R., Lungren, M.P., Deng, C.Y., Peng, Y., Lu, Z., Mark, R.G., Berkowitz, S.J., Horng, S., 2019b. Mimic-cxr-jpg, a large publicly available database of labeled chest radiographs. arXiv preprint arXiv:1901.07042.
- Karthik, Maggie, S.D., 2019. Aptos 2019 blindness detection. URL: <https://kaggle.com/competitions/aptos2019-blindness-detection>.
- Krizhevsky, A., Sutskever, I., Hinton, G.E., 2017. Imagenet classification with deep convolutional neural networks. Communications of the ACM 60, 84–90.
- Li, C.Y., Liang, X., Hu, Z., Xing, E.P., 2019. Knowledge-driven encode, retrieve, paraphrase for medical image report generation, in: AAAI, pp. 6666–6673.
- Li, J., Li, D., Xiong, C., Hoi, S., 2022a. Blip: Bootstrapping language-image pre-training for unified vision-language understanding and generation, in: International Conference on Machine Learning, PMLR. pp. 12888–12900.
- Li, J., Selvaraju, R., Gotmare, A., Joty, S., Xiong, C., Hoi, S.C.H., 2021a. Align before fuse: Vision and language representation learning with momentum distillation. Advances in neural information processing systems 34, 9694–9705.
- Li, L.H., Zhang, P., Zhang, H., Yang, J., Li, C., Zhong, Y., Wang, L., Yuan, L., Zhang, L., Hwang, J.N., et al., 2022b. Grounded language-image pre-training, in: Proceedings of the IEEE/CVF Conference on Computer Vision and Pattern Recognition, pp. 10965–10975.
- Li, M., Cai, W., Liu, R., Weng, Y., Zhao, X., Wang, C., Chen, X., Liu, Z., Pan, C., Li, M., et al., 2021b. Ffa-ir: Towards an explainable and reliable medical report generation benchmark, in: Thirty-fifth conference on neural information processing systems datasets and benchmarks track (round 2).
- Li, W., Gao, C., Niu, G., Xiao, X., Liu, H., Liu, J., Wu, H., Wang, H., 2020a. Unimo: Towards unified-modal understanding and generation via cross-modal contrastive learning. arXiv preprint arXiv:2012.15409.
- Li, X., Yin, X., Li, C., Zhang, P., Hu, X., Zhang, L., Wang, L., Hu, H., Dong, L., Wei, F., et al., 2020b. Oscar: Object-semantics aligned pre-training for vision-language tasks, in: ECCV, pp. 121–137.
- Li, Y., Fan, H., Hu, R., Feichtenhofer, C., He, K., 2022c. Scaling language-image pre-training via masking. arXiv preprint arXiv:2212.00794.
- Li, Y., Liang, X., Hu, Z., Xing, E.P., 2018. Hybrid retrieval-generation reinforced agent for medical image report generation, in: NeurIPS.
- Li, Z., Yang, L.T., Ren, B., Nie, X., Gao, Z., Tan, C., Li, S.Z., 2024. Mlip: Enhancing medical visual representation with divergence encoder and knowledge-guided contrastive learning, in: Proceedings of the IEEE/CVF Conference on Computer Vision and Pattern Recognition, pp. 11704–11714.
- Lipscomb, C.E., 2000. Medical subject headings (mesh). Bulletin of the Medical Library Association 88, 265.
- Liu, B., Lu, D., Wei, D., Wu, X., Wang, Y., Zhang, Y., Zheng, Y., 2023a. Improving medical vision-language contrastive pretraining with semantics-aware triage. IEEE Transactions on Medical Imaging.
- Liu, F., Zhu, T., Wu, X., Yang, B., You, C., Wang, C., Lu, L., Liu, Z., Zheng, Y., Sun, X., et al., 2023b. A medical multimodal large language model for future pandemics. NPJ Digital Medicine 6, 226.
- Loshchilov, I., Hutter, F., 2017. Decoupled weight decay regularization. arXiv preprint arXiv:1711.05101.
- Min, S., Lyu, X., Holtzman, A., Artetxe, M., Lewis, M., Hajishirzi, H., Zettlemoyer, L., 2022. Rethinking the role of demonstrations: What makes in-context learning work?, pp. 11048–11064.
- Mu, N., Kirillov, A., Wagner, D., Xie, S., 2022. Slip: Self-supervision meets language-image pre-training, in: European Conference on Computer Vision, Springer. pp. 529–544.
- OpenAI, 2023. Gpt-4 technical report. arXiv preprint arXiv:2303.08774.
- Ouyang, L., Wu, J., Jiang, X., Almeida, D., Wainwright, C., Mishkin, P., Zhang, C., Agarwal, S., Slama, K., Ray, A., et al., 2022. Training language models to follow instructions with human feedback, pp. 27730–27744.
- Paszke, A., Gross, S., Massa, F., Lerer, A., Bradbury, J., Chanan, G., Killeen, T., Lin, Z., Gimelshein, N., Antiga, L., et al., 2019. Pytorch: An imperative style, high-performance deep learning library. Advances in neural information processing systems 32.
- Pathak, Y., Shukla, P.K., Tiwari, A., Stalin, S., Singh, S., 2022. Deep transfer learning based classification model for covid-19 disease. Irbm 43, 87–92.
- Pellegrini, C., Keicher, M., Özsoy, E., Jiraskova, P., Braren, R., Navab, N., 2023. Xplainer: From x-ray observations to explainable zero-shot diagnosis.
- Radford, A., Kim, J.W., Hallacy, C., Ramesh, A., Goh, G., Agarwal, S., Sastry, G., Askell, A., Mishkin, P., Clark, J., et al., 2021. Learning transferable visual models from natural language supervision, in: International Conference on Machine Learning, PMLR. pp. 8748–8763.
- Rodríguez, M.A., AlMarzouqi, H., Liatsis, P., 2022. Multi-label retinal disease classification using transformers. IEEE Journal of Biomedical and Health Informatics 27, 2739–2750.
- Sanh, V., Webson, A., Raffel, C., Bach, S.H., Sutawika, L., Alyafeai, Z., Chaffin, A., Stiegler, A., Le Scao, T., Raja, A., et al., 2022. Multitask prompted training enables zero-shot task generalization, in: ICLR.
- Shih, G., Wu, C.C., Halabi, S.S., Kohli, M.D., Prevedello, L.M., Cook, T.S., Sharma, A., Amorosa, J.K., Arteaga, V., Galperin-Aizenberg, M., et al., 2019. Augmenting the national institutes of health chest radiograph dataset with expert annotations of possible pneumonia. Radiology: Artificial Intelligence 1, e180041.
- Silva-Rodríguez, J., Chakor, H., Kobbi, R., Dolz, J., Ayed, I.B., 2023. A foundation language-image model of the retina (flair): Encoding expert knowledge in text supervision. arXiv preprint arXiv:2308.07898.
- Steven G. Langer, PhD, C., George Shih, MD, M., 2019. Siim-acr pneumothorax segmentation.
- Su, C.Y., Mcmillan, C., 2023. Distilled gpt for source code summarization. arXiv:2308.14731.
- Titano, J.J., Badgeley, M., Schefflein, J., Pain, M., Su, A., Cai, M., Swinburne, N., Zech, J., Kim, J., Bederson, J., et al., 2018. Automated deep-neural-network surveillance of cranial images for acute neurologic events. Nature medicine 24, 1337–1341.
- Tiu, E., Talus, E., Patel, P., Langlotz, C.P., Ng, A.Y., Rajpurkar, P., 2022. Expert-level detection of pathologies from unannotated chest x-ray images via self-supervised learning. Nature Biomedical Engineering 6, 1399–1406.
- Wan, Z., Liu, C., Zhang, M., Fu, J., Wang, B., Cheng, S., Ma, L., Quilodrán-Casas, C., Arcucci, R., 2023. Med-unic: Unifying cross-lingual medical vision-language pre-training by diminishing bias, in: NeurIPS.
- Wang, F., Zhou, Y., Wang, S., Vardhanabhuti, V., Yu, L., 2022. Multi-granularity cross-modal alignment for generalized medical visual representation learning.
- Wang, L., Lin, Z.Q., Wong, A., 2020. Covid-net: A tailored deep convolutional neural network design for detection of covid-19 cases from chest x-ray images. Scientific reports 10, 1–12.
- Wang, X., Peng, Y., Lu, L., Lu, Z., Bagheri, M., Summers, R.M., 2017. Chestx-ray8: Hospital-scale chest x-ray database and benchmarks on weakly-supervised classification and localization of common thorax diseases, in: Proceedings of the IEEE conference on computer vision and pattern recognition, pp. 2097–2106.
- Wang, Z., Yu, J., Yu, A.W., Dai, Z., Tsvetkov, Y., Cao, Y., . Simvlm: Simple visual language model pretraining with weak supervision, in: International Conference on Learning Representations.
- Wei, J., Bosma, M., Zhao, V., Guu, K., Yu, A.W., Lester, B., Du, N., Dai, A.M., Le, Q.V., 2021. Finetuned language models are zero-shot learners, in: ICLR.
- Wu, C., Zhang, X., Zhang, Y., Wang, Y., Xie, W., 2023. Medklip: Medical knowledge enhanced language-image pre-training, in: ICCV.
- Wu, Y., Schuster, M., Chen, Z., Le, Q.V., Norouzi, M., Macherey, W., Krikun, M., Cao, Y., Gao, Q., Macherey, K., et al., 2016. Google’s neural machine

- translation system: Bridging the gap between human and machine translation. arXiv preprint arXiv:1609.08144 .
- Xie, Y., Chen, Q., Wang, S., To, M.S., Lee, I., Khoo, E.W., Hendy, K., Koh, D., Xia, Y., Wu, Q., 2024a. Pairaug: What can augmented image-text pairs do for radiology?, in: *Proceedings of the IEEE/CVF Conference on Computer Vision and Pattern Recognition*, pp. 11652–11661.
- Xie, Y., Gu, L., Harada, T., Zhang, J., Xia, Y., Wu, Q., 2023. Medim: Boost medical image representation via radiology report-guided masking, Springer. pp. 13–23.
- Xie, Y., Gu, L., Harada, T., Zhang, J., Xia, Y., Wu, Q., 2024b. Rethinking masked image modeling for medical image representation. *Medical Image Analysis* , 103304URL: <https://www.sciencedirect.com/science/article/pii/S1361841524002299>, doi:<https://doi.org/10.1016/j.media.2024.103304>.
- Ye, Y., Xie, Y., Zhang, J., Chen, Z., Wu, Q., Xia, Y., 2024. Continual self-supervised learning: Towards universal multi-modal medical data representation learning, in: *Proceedings of the IEEE/CVF Conference on Computer Vision and Pattern Recognition*, pp. 11114–11124.
- Zhang, K., Yang, Y., Yu, J., Jiang, H., Fan, J., Huang, Q., Han, W., 2023a. Multi-task paired masking with alignment modeling for medical vision-language pre-training. *IEEE Transactions on Multimedia* .
- Zhang, P., Li, X., Hu, X., Yang, J., Zhang, L., Wang, L., Choi, Y., Gao, J., 2021. Vinvl: Revisiting visual representations in vision-language models, in: *CVPR*, pp. 5579–5588.
- Zhang, T., Ladhak, F., Durmus, E., Liang, P., McKeown, K., Hashimoto, T.B., 2023b. Benchmarking large language models for news summarization. arXiv preprint arXiv:2301.13848 .
- Zhang, X., Wu, C., Zhang, Y., Xie, W., Wang, Y., 2023c. Knowledge-enhanced visual-language pre-training on chest radiology images. *Nature Communications* 14, 4542.
- Zhang, Y., Jiang, H., Miura, Y., Manning, C.D., Langlotz, C.P., 2020. Contrastive learning of medical visual representations from paired images and text. arXiv preprint arXiv:2010.00747 .
- Zhou, H.Y., Chen, X., Zhang, Y., Luo, R., Wang, L., Yu, Y., 2022. Generalized radiograph representation learning via cross-supervision between images and free-text radiology reports. *Nature Machine Intelligence* 4, 32–40.
- Zhou, H.Y., Lian, C., Wang, L., Yu, Y., 2023a. Advancing radiograph representation learning with masked record modeling, in: *ICLR*.
- Zhou, S.K., Greenspan, H., Davatzikos, C., Duncan, J.S., Van Ginneken, B., Madabhushi, A., Prince, J.L., Rueckert, D., Summers, R.M., 2021. A review of deep learning in medical imaging: Imaging traits, technology trends, case studies with progress highlights, and future promises. *Proceedings of the IEEE* .
- Zhou, Y., Chia, M.A., Wagner, S.K., Ayhan, M.S., Williamson, D.J., Struyven, R.R., Liu, T., Xu, M., Lozano, M.G., Woodward-Court, P., et al., 2023b. A foundation model for generalizable disease detection from retinal images. *Nature* 622, 156–163.